The Astrophysical Journal, 1000:13 (13pp), 2026 March 20 https://doi.org/10.3847/1538-4357/ae3c7b

Correlation between Electron Temperature and Ion Charge-state Ratios in the Solar Wind at ∼0.5 au

Xiangyu Wu (吴翔宇)[1,6], Christopher J. Owen[1], Jesse Coburn[2], Georgios Nicolaou[1], Daniel Verscharen[1], Jingting Liu (刘婧婷)[1], Charalambos Ioannou[1], Hao Ran (冉豪)[1], Yeimy J. Rivera[3], and Stephanie L. Yardley[1,4,5]
[1] Mullard Space Science Laboratory, University College London, Dorking, Surrey RH5 6NT, UK; xiangyu.wu.23@ucl.ac.uk
[2] The Blackett Laboratory, Imperial College London, London, SW7 2AZ, UK
[3] Center for Astrophysics|Harvard & Smithsonian, 60 Garden Street, Cambridge, MA 02138, USA
[4] Department of Mathematics, Physics and Electrical Engineering, Northumbria University, Ellison Place, Newcastle Upon Tyne, NE1 8ST, UK
[5] Donostia International Physics Center (DIPC), Paseo Manuel de Lardizabal 4, 20018, San Sebastián, Spain
Received 2025 October 30; revised 2026 January 19; accepted 2026 January 20; published 2026 March 10

Abstract

Whether solar wind electrons expanding into the heliosphere can preserve information about their origin in the solar corona remains an open debate. The suprathermal strahl temperature has often been postulated as an indicator of source coronal electron temperature, while the core electron temperature has also been found to correlate with the solar wind velocity in the inner heliosphere. Here we investigate how well solar wind electron populations retain imprints of coronal electron temperature. Using Solar Orbiter measurements at ∼0.5 au, we fit three components (i.e., the core, halo, and strahl) of the electron velocity distribution function and compare the resulting strahl and core temperatures with heavy-ion charge-state ratios, which serve as proxies for the coronal electron temperature. We present the first clear evidence from inner heliosphere observations that, in several individual streams, a proxy for the strahl parallel temperature, $T_{\mathrm{strahl},\parallel}$, correlates significantly and positively with the charge-state ratios O^{7+}/O^{6+} and C^{6+}/C^{5+}. However, this correlation is not universally present, implying that many electron streams are significantly affected by transport processes, such as scattering, that erase the signature. We find that, notably, the core perpendicular temperature ($T_{\mathrm{core},\perp}$) also strongly correlates with the charge-state ratios. We interpret this result within the framework of the exospheric solar wind model. Our results suggest that both thermal and suprathermal electrons can at times retain coronal information, but that aggregating multiple streams can obscure the underlying relationships.

Unified Astronomy Thesaurus concepts: Solar wind (1534); Space plasmas (1544); Interplanetary physics (827)

1. Introduction

The solar wind is the continuous outflow of plasma from the solar corona, carrying the magnetic field of solar origin with it. Solar wind electrons consist of three major components, known as the core, halo, and strahl (W. C. Feldman et al. 1975; W. G. Pilipp et al. 1987). The core population, found at lower energies, accounts for ∼90%–95% of the total electron density and can often be described by a bi-Maxwellian distribution (W. C. Feldman et al. 1975; M. Maksimovic et al. 1997). At higher energies, where Coulomb collisions are less frequent, the electron velocity distribution function (VDF) shows non-Maxwellian features. The halo population exhibits a higher temperature and lower density than the core, and the VDF at these velocities displays a power-law shape. The halo is thus often modeled using a bi-κ distribution (M. Maksimovic et al. 1997, 2005; Š. Štverák et al. 2009). The strahl population (∼100–1000 eV) appears as a field-aligned shoulder on the VDF, moving parallel or antiparallel to the magnetic field at velocities significantly exceeding the plasma bulk speed (W. C. Feldman et al. 1978; W. G. Pilipp et al. 1987). The shape of the strahl VDF has a radial dependence and can be modeled by a bi-Maxwellian or bi-κ distribution (W. C. Feldman et al. 1978; W. G. Pilipp et al. 1987; Š. Štverák et al. 2009; L. Berčič et al. 2020).

The exospheric model of the solar wind provides a kinetic description of these electron populations in interplanetary space. It assumes collisionless transport above an exobase, which is defined as the radial distance at which the electron mean free path exceeds the density scale height (J. Lemaire & M. Scherer 1971; V. Pierrard & J. Lemaire 1996; N. Meyer-Vernet & K. Issautier 1998; M. Maksimovic et al. 2001; S. Boldyrev et al. 2020). At this distance, the relatively light electrons, free from collisions, can stream ahead of the ions, generating an ambipolar electric field. Figure 1, adapted from S. Boldyrev et al. (2020), shows an idealized electron VDF expected on the basis of a standard exospheric model. Escaping electrons with energy higher than the asymptotic ambipolar potential energy (green shaded region in Figure 1) stream outward to infinity, are adiabatically focused along the field direction and contribute to the strahl population. Electrons with kinetic energy lower than the ambipolar potential (defining the velocity represented by the dashed circle) will eventually be reflected. These electrons, and their counterparts returning to the collisional coronal reservoir, are called ballistic electrons (yellow shaded region). Finally, electrons confined between a near-Sun magnetic mirror and a distant ambipolar potential barrier are the trapped electrons (orange shaded region). Ballistic and trapped electrons combined contribute to the core electron population. The halo may be formed by electrons scattered out of the strahl, as suggested by the anticorrelation between the variation of

[6] Corresponding author.

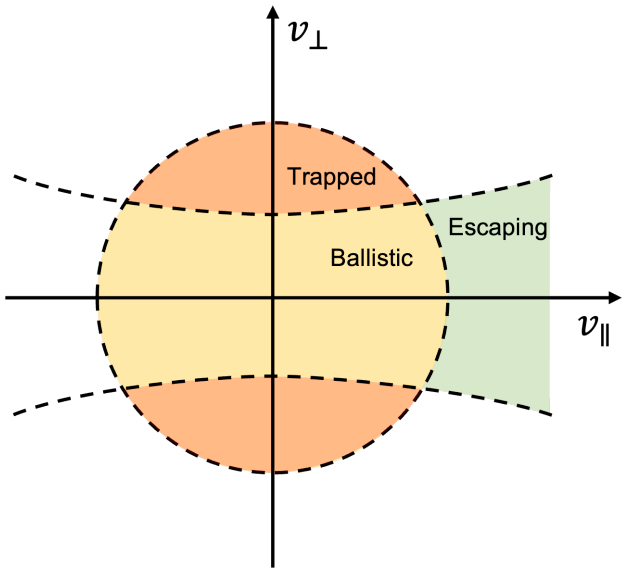

Figure 1. A schematic diagram of the electron VDF from an exospheric model. The *x*-axis is the parallel velocity, and the *y*-axis is the perpendicular velocity with respect to the magnetic field direction. Ballistic, trapped, and escaping electron populations are marked by yellow, orange, and green. After S. Boldyrev et al. (2020).

fractional densities of the halo and strahl with increasing radial density (M. Maksimovic et al. 2005; Š. Štverák et al. 2009). However, many studies conversely suggest the halo cannot be formed simply from the scattering of the strahl. Other processes in the corona, or acting during the transit, may also contribute to the growth of halo population (V. Pierrard et al. 1999; H. Che & M. L. Goldstein 2014; J. B. Abraham et al. 2022).

Escaping electrons (i.e., the strahl) are often assumed to retain signatures of their coronal origin (W. C. Feldman et al. 1975). Under adiabatic, scatterfree motion, conservation of the magnetic moment focuses the strahl toward smaller pitch angles as the magnetic field decreases, while preserving the field-aligned VDF shape. Therefore, in the field-aligned direction, strahl electrons may carry information about the coronal electrons at the solar wind source. Recent observations in the inner heliosphere indicate that imprints of solar wind's coronal origin remain apparent close to the Sun. Using Parker Solar Probe (PSP) measurements within 0.25 au, J. S. Halekas et al. (2020) report clear anticorrelations between solar wind bulk speed (V_{sw}) and both core and halo temperatures. Combining PSP's measurements with Helios, Wind, and Ulysses datasets, M. Maksimovic et al. (2020a) show that this strong anticorrelation, prominent around 0.15 au, disappears as solar wind expands, evolves, and mixes. At 1 au, C. S. Salem et al. (2023) perform a comprehensive analysis of electron VDFs measured by the Wind spacecraft over four years and confirm that electron temperatures (T_e) are generally lower in fast wind than in slow wind, with the T_e–V_{sw} relationship highly variable in slow wind but anticorrelated in fast wind. This radial degradation of the anticorrelation between T_e–V_{sw} suggests that processes such as collisions, wave–particle interactions, and turbulence (C. Vocks et al. 2005; C. Pagel et al. 2007; K. Horaites et al. 2019) may progressively modify the electron VDF, eroding signatures of the coronal source.

One practical way to investigate whether the measured electrons actually preserve signatures about their coronal origin is through comparison to the heavy-ion charge-state ratios, which provide an independent diagnostic of coronal properties, in particular its electron temperature. The heavy-ion charge-state distribution in the solar wind is established in the corona and is known to remain unchanged as the plasma propagates outward (A. J. Hundhausen et al. 1968; S. P. Owocki et al. 1983; P. Bochsler 2007; E. Landi et al. 2012b; Y. J. Rivera et al. 2022). The charge states are determined by the competition of two timescales, the charge modification timescale and the expansion timescale (Y.-K. Ko et al. 1997; S. Hefti et al. 2000; V. Heidrich-Meisner et al. 2016), which are controlled by the electron temperature, density profile of the corona and the outflow velocity. Ion charge states continue to evolve while the charge modification timescale is shorter than the expansion timescale. However, once the ions reach an altitude where the ambient electron density is not sufficient for further ionization or recombination, the charge-state distribution is "frozen in" and subsequently convected into interplanetary space. The species-dependent "freeze-in" height is typically between 1.5 and 10 R_{Sun} in the corona (Y.-K. Ko et al. 1997; Y. Chen et al. 2003; E. Landi et al. 2012a; B. Boe et al. 2018; R. Lionello et al. 2019; Y. J. Rivera et al. 2022; J. Szente et al. 2022; P. Riley et al. 2025). The resulting charge-state ratio therefore provides a well-established proxy for the local electron temperature near the freeze-in height, under the assumption of ionization equilibrium. If this assumption is violated, the ions instead reflect the coupled evolution of electron temperature, density, and velocity up to the freeze-in point, and thus represent a more ambiguous, but still valuable marker, of the coronal thermal structure. If solar wind electrons truly retain that coronal signature, their temperature would be expected to correlate with the frozen-in charge-state ratio. Among available diagnostics, the oxygen charge-state ratio O^{7+}/O^{6+}, defined as the ratio of the number density of O^{7+} ions to that of O^{6+}, is especially useful (Y.-K. Ko et al. 2014), being both abundant in the solar wind and highly sensitive to the electron temperature at the coronal source (R. Esser & R. J. Edgar 2000).

Existing studies of the relationship between electrons and O^{7+}/O^{6+} are mainly based on datasets at 1 au. S. Hefti et al. (1999) report a clear correlation between the effective suprathermal electron temperature (T_{eff}) and the O^{7+}/O^{6+} ratio during two intervals, using WIND and ACE measurements. In that work, T_{eff} is a representative of the suprathermal electron temperature at a given energy, defined as the differential of a Maxwellian distribution ($T_{eff} = [k_B(d \ln f/dE)]^{-1}$, where k_B is the Boltzmann constant, f is the electron VDF, and E is energy). Extending this analysis over 14 yr, A. R. Macneil et al. (2017) conversely find that the temperature of suprathermal electrons at 1 au has little to no residual signature of the coronal electron temperature at their source. They find numerous subsets of data, some showing significant correlation between the suprathermal electron temperature and O^{7+}/O^{6+} charge-state ratio while others show none, demonstrating that the correlation may vary from stream to stream. A more recent study using measurements from the Parker Solar Probe and Helios missions (L. Berčič et al. 2020) finds that strahl parallel temperature is independent of radial distance and that its variation is broadly consistent with the coronal features inferred from remote-sensing observations, supporting the hypothesis that strahl electrons may carry coronal electron temperature information.

In this study, we exploit Solar Orbiter (SO) observations that are taken at closer radial distances, ~0.5 au, than previous

studies and thus may be less affected by transport effects, to investigate whether the temperatures of electron components correlate with heavy-ion charge-state ratios when both are measured in situ and within the same solar wind stream. Specifically, we obtain two diagnostics from fits to the electron VDF: the core perpendicular temperature ($T_{\mathrm{core},\perp}$) and a velocity-moment-based proxy for the strahl parallel temperature ($T_{\mathrm{strahl},\parallel}$). We then examine how they vary with charge-state ratios across the interval studied.

2. Datasets and Methodology

2.1. Datasets

In situ measurements used in this study are provided by SO and are available from the Solar Orbiter Archive (SOAR). The solar wind plasma is measured by the Solar Wind Analyser (SWA) suite, consisting of three sensors (C. J. Owen et al. 2020). The Electron Analyser System (SWA-EAS) consists of two orthogonally mounted top-hat electrostatic analyzers. Each head measures the electron velocity distribution functions over 64 energy bins (from a few eV to ∼5 keV), 32 azimuth bins, and 16 stepped elevation bins, deflecting incoming electrons by ±45° in elevation and offering 360° azimuthal coverage. The two heads provide a combined field of view (FoV) of the full sky. In this study, we use the normal mode EAS Level-1 electron Counts and Level-2 Phase Space Density (PSD) data, sampling the 3D VDF at 1 s resolution and downlinked every 10 s. The solar wind proton velocity is provided by the Proton and Alpha particle Sensor (SWA-PAS), which measures the 3D VDF of solar wind protons and α-particles using an electrostatic analyzer, from which bulk moments (density, velocity, and pressure) are derived. PAS provides a 66°(azimuth) × ± 22.°5(elevation) FoV, and scans the energy range from 200 eV/q to 20 keV/e every 4 s for the periods used in this study. The Heavy Ion Sensor (HIS) measures the 3D VDFs of heavy ions (e.g., He, C, O, Fe) over an energy range of 0.5–80 keV/e. It has a FoV spanning −33° to +66° in azimuth (in the ecliptic) and ±17° in elevation (out of the ecliptic). We use its Level-3 10 minute data products that include the oxygen (O^{7+}/O^{6+}) and carbon (C^{6+}/C^{5+}) charge-state ratios. The magnetic field vectors used to rotate the electron VDFs to a magnetic field-aligned frame are provided by the Magnetometer (MAG) instrument, measuring the vector magnetic field at 16 vectors s^{-1} (T. S. Horbury et al. 2020). The floating spacecraft potential (ϕ_{sc}) estimates used to correct the SWA-EAS electron energy channel are provided by the Radio and Plasma Waves (RPW) instrument (M. Maksimovic et al. 2020b).

2.2. Models

We shift the electron VDF to the plasma rest frame by subtracting the solar wind proton velocity in the SO spacecraft frame (SRF), and reorganize the electron VDF into a magnetic field-aligned frame, using field measurements from MAG in the SRF frame. Then, we fit the VDF to a distribution made up of the sum of three analytical models that describe the three components (i.e., core, halo, and strahl) in the solar wind:

$$f_e = f_{\mathrm{core}} + f_{\mathrm{halo}} + f_{\mathrm{strahl}}. \quad (1)$$

The core population, f_{core}, is modeled by a bi-Maxwellian distribution drifting in the parallel direction with respect to the magnetic field (Š. Štverák et al. 2009; L. Berčič et al. 2020; J. B. Abraham et al. 2022):

$$f_{\mathrm{core}} = \frac{n_c}{\pi^{3/2} v_{\parallel \mathrm{th,c}} v_{\perp \mathrm{th,c}}^2} \exp\left(-\left(\frac{v_\parallel - u_{\parallel,c}}{v_{\parallel \mathrm{th,c}}} \right)^2 - \left(\frac{v_\perp}{v_{\perp \mathrm{th,c}}} \right)^2 \right) \quad (2)$$

where n_c is the core density, and $u_{\parallel,c}$ is the parallel drift velocity of the core. We define the thermal speeds, $v_{\parallel \mathrm{th,c}}$ and $v_{\perp \mathrm{th,c}}$, parallel and perpendicular to the magnetic field by $v_{(\parallel,\perp)\mathrm{th,c}} = \sqrt{2 k_{\mathrm{B}} T_c / m_e}$, where k_{B} is Boltzmann's constant, $T_{c(\parallel,\perp)}$ is the core temperature, and m_e is the electron mass. $v_\parallel$ and $v_\perp$ represent electron velocities parallel and perpendicular to the magnetic field direction.

For the suprathermal components, namely halo and strahl, we adopt the models proposed by Š. Štverák et al. (2009). The halo population is described by a modified bi-κ distribution, in which the low-energy part of the bi-κ function is suppressed by a flat-top function ($f_{\mathrm{halo,ft}}$) where the thermal core dominates. The form for the halo is

$$f_{\mathrm{halo}} = (1 - f_{\mathrm{halo,ft}}) f_{\mathrm{halo},\kappa} \quad (3)$$

where the $f_{\mathrm{halo},\kappa}$ is a bi-κ distribution:

$$f_{\mathrm{halo},\kappa} = \frac{n_h}{\pi^{3/2} v_{\parallel \mathrm{th,h}} v_{\perp \mathrm{th,h}}^2 (\kappa_h - 3/2)^{3/2}} \frac{\Gamma(\kappa_h + 1)}{\Gamma(\kappa_h - 1/2)} \times \left(1 + \frac{1}{(\kappa_h - 3/2)} \left[\left(\frac{v_\parallel - u_{\parallel,h}}{v_{\parallel \mathrm{th,h}}} \right)^2 + \left(\frac{v_\perp}{v_{\perp \mathrm{th,h}}} \right)^2 \right] \right)^{-\kappa_h - 1} \quad (4)$$

n_h is the halo density, $v_{\parallel \mathrm{th,h}}$ is the halo parallel thermal velocity, $v_{\perp \mathrm{th,h}}$ is the halo perpendicular thermal velocity, $u_{\parallel,h}$ is the parallel drift velocity of halo, $\Gamma(x)$ is the Gamma function, and κ_h is the κ index controlling the density of the high-energy portion of the VDF. The "flat-top" function $f_{\mathrm{halo,ft}}$ is defined as

$$f_{\mathrm{halo,ft}} = \left(1 + \frac{1}{\delta} \left(\frac{(v_\parallel - u_{\parallel,c})^2}{v_{\parallel \mathrm{th,c}}^2} + \frac{v_\perp^2}{v_{\perp \mathrm{th,c}}^2} \right)^p \right)^{-q} \quad (5)$$

where δ is the width of the flat top. This function creates a plateau symmetric with respect to the origin. With increasing velocity, $f_{\mathrm{halo,ft}}$ falls rapidly to zero. The shape of the edge of the plateau is controlled by constant parameters p and q. We follow Š. Štverák et al. (2009) and set the truncation exponents to values $p = 10$ and $q = 1$, which are steep enough to ensure an effective cutoff of the VDF.

The strahl component is also described by a truncated bi-κ distribution form:

$$f_{\mathrm{strahl}} = \frac{2 n_s \sqrt{\Theta}}{\pi^{3/2} v_{\parallel \mathrm{th,s}} v_{\perp \mathrm{th,s}}^2 \sqrt{\Theta + 1} (\kappa_s - 3/2)^{3/2}} \frac{\Gamma(\kappa_s + 1)}{\Gamma(\kappa_s - 1/2)} \times \left(1 + \frac{1}{(\kappa_s - 3/2)} \left[D \left(\frac{v_\parallel - u_{\parallel,s}}{v_{\parallel \mathrm{th,s}}} \right)^2 + \left(\frac{v_\perp}{v_{\perp \mathrm{th,s}}} \right)^2 \right] \right)^{-\kappa_s - 1} \quad (6)$$

with

$$D = 1, \quad \text{if} \quad v_{\parallel} \geqslant u_{\parallel,s}$$
$$D = \Theta, \quad \text{if} \quad v_{\parallel} < u_{\parallel,s} \tag{7}$$

where n_s gives the strahl number density, $u_{\parallel,s}$ is the parallel drift velocity of the strahl, $v_{\parallel \mathrm{th,s}}$ and $v_{\perp \mathrm{th,s}}$ are thermal velocities of strahl in parallel and perpendicular directions, and κ_s is the κ index of the strahl VDF. Θ and D are two parameters that modify the bi-κ function to only model the high-energy tail of the measured electron VDF (Š. Štverák et al. 2009). Specifically, Θ controls the steepness of the f_{strahl} decline, and D acts as a conditional switch that controls where the cutoff starts. Equation (7) ensures that the function is only truncated near the thermal energy range, while maintaining a classic bi-κ form for higher energy zones. We evaluate Θ using synthetic VDFs and verify that fixing $\Theta = 10$ during the fitting is sufficient to cut off the f_{strahl} in the thermal core energy range, consistent with Š. Štverák et al. (2009).

2.3. Electron VDF Fitting

The fit of data to our model involves 15 free parameters (n_c, n_h, n_s, $v_{\parallel \mathrm{th,c}}$, $v_{\perp \mathrm{th,c}}$, $v_{\parallel \mathrm{th,h}}$, $v_{\perp \mathrm{th,h}}$, $v_{\parallel \mathrm{th,s}}$, $v_{\perp \mathrm{th,s}}$, $u_{\parallel c}$, $u_{\parallel h}$, $u_{\parallel s}$, κ_h, κ_s, and δ). To achieve a good fit, we process the data in three steps:

(1) We first compute the electron pitch-angle distribution (PAD) by assigning each EAS VDF measurement to one of 18 pitch-angle bins (10° width), using the angle between the electron velocity vector and the local magnetic field measured by MAG in the SRF frame. We then average the resulting PAD over energies from 50 to 2000 eV and fit it with the model proposed by C. J. Owen et al. (2022):

$$f(\alpha) = P_B + P_0 \exp\left(-\frac{\alpha^2}{1.45\ W_0^2}\right) + P_{180} \exp\left(-\frac{(\alpha - 180°)^2}{1.45\ W_{180}^2}\right) \tag{8}$$

where α represents pitch angle, P_B is a constant background, P_0 and W_0 are the height and full width at half-maximum (FWHM) of a Gaussian centered at the field-aligned ($\alpha = 0°$) direction, P_{180} and W_{180} are the height and FWHM of a Gaussian centered at the anti-field-aligned ($\alpha = 180°$) direction. This model helps determine the direction and pitch-angle width of the strahl population.

(2) Initial fitting phase: to reduce dimensionality, we fit each electron component, i.e., core, halo, and strahl, independently and use those results as initial estimates for the final fit. To roughly identify the energy boundary between the thermal core and suprathermal electrons, we apply a K-means clustering technique that has already been validated to obtain the break energy between these two populations (M. R. Bakrania et al. 2020; J. B. Abraham et al. 2022). The K-means algorithm clusters data points by minimizing the sum of squared Euclidean distances to their cluster centroids. In practice, it begins with N (number of groups) random centroids, then alternates between assigning each point to its nearest centroid and updating each centroid to the mean of its assigned points. This process repeats until assignments no longer change. In our study, K-means is applied to the electron VDF in the field-aligned frame with pitch angles between 80° and 100°, thereby avoiding the strahl. The electron VDF is limited to above 15 eV to minimize contamination from spacecraft-emitted electrons at low energies (G. Nicolaou et al. 2021; Š. Štverák et al. 2025). For the remaining VDF, we correct the electron energies by subtracting the ϕ_{sc} measured by RPW. The corrected VDF is then clustered into two groups, corresponding to the core and suprathermal components. The core is fitted over $15 - \phi_{\mathrm{sc}}$ eV to the break energy at all pitch angles. Then, using the direction and width of strahl from step (1), we fit the halo to the VDF outside the strahl cone with energy above the break energy; we fit the strahl to measurements where the strahl appears and with energy between the break energy and 1000 eV. Note that although we carefully select data to include only one electron component, the resulting separation may not be exact. However, our multistep fitting approach prevents overreliance on the break energy and the PAD fitting by using the initial fitting results only as inputs for the final fit.

(3) Final fitting phase: the parameters obtained from the initial fits are used as starting points for the combined model (Equation (1)), and all 15 parameters are then adjusted simultaneously.

The goodness of fit is quantified by comparing modeled points with measured data, using the reduced χ^2_{red} parameter:

$$\chi^2_{\mathrm{red}} = \frac{1}{N - m} \sum_{i}^{N} \frac{(O_i - M_i)^2}{\sigma_i^2} \tag{9}$$

where $O_i = \log(f_i)$ is the logarithm of the measured electron VDFs, $M_i = \log(f_{\mathrm{fit}})$ is the logarithm of the fitted VDF data, N is the number of data points for the fit, m is the number of free parameters to fit, and σ_i is the uncertainty of the VDF measurements. The observed VDF value f_i is derived from EAS electron counts, C_i:

$$f_i = \frac{m_e^2 C_i}{2 \Delta t E_i^2 G_i Q_{E_i}} \tag{10}$$

where m_e is the mass of electrons, Δt is the counter readout time, G_i is the geometric factor for the specific bin, E_i represents the corresponding energy, Q_{E_i} is the quantum efficiency of the detector, and C_i is the detected number of counts. When a detector measures the particle flux, the probability of an individual measurement of particles in a specific interval, is given by the Poisson distribution (P. Bevington & D. K. Robinson 2003), and the standard deviation of the Poisson distribution is $\sqrt{C_i}$. We consider the uncertainty of each count measurement $\sigma(C_i) = \sqrt{C_i}$, a direct outcome of the Poisson statistics, and propagate this to the PSD data to obtain σ_i through Equation (10). We then compute χ^2_{red} via Equation (9). A value of $\chi^2_{\mathrm{red}} \simeq 1$ indicates that the final fit of the model to the measured data is consistent with the expected standard deviation of the measured distribution. In this study, we retain only fits with $0.6 \leqslant \chi^2_{\mathrm{red}} \leqslant 1.2$, thereby excluding solutions that either underrepresent the VDF (underfitting) or overinterpret the noise and random fluctuations (overfitting).

The fits are implemented using the *lmfit* Python package (M. Newville et al. 2016), which builds on SciPy's optimization routines and adds functionality tailored to complex

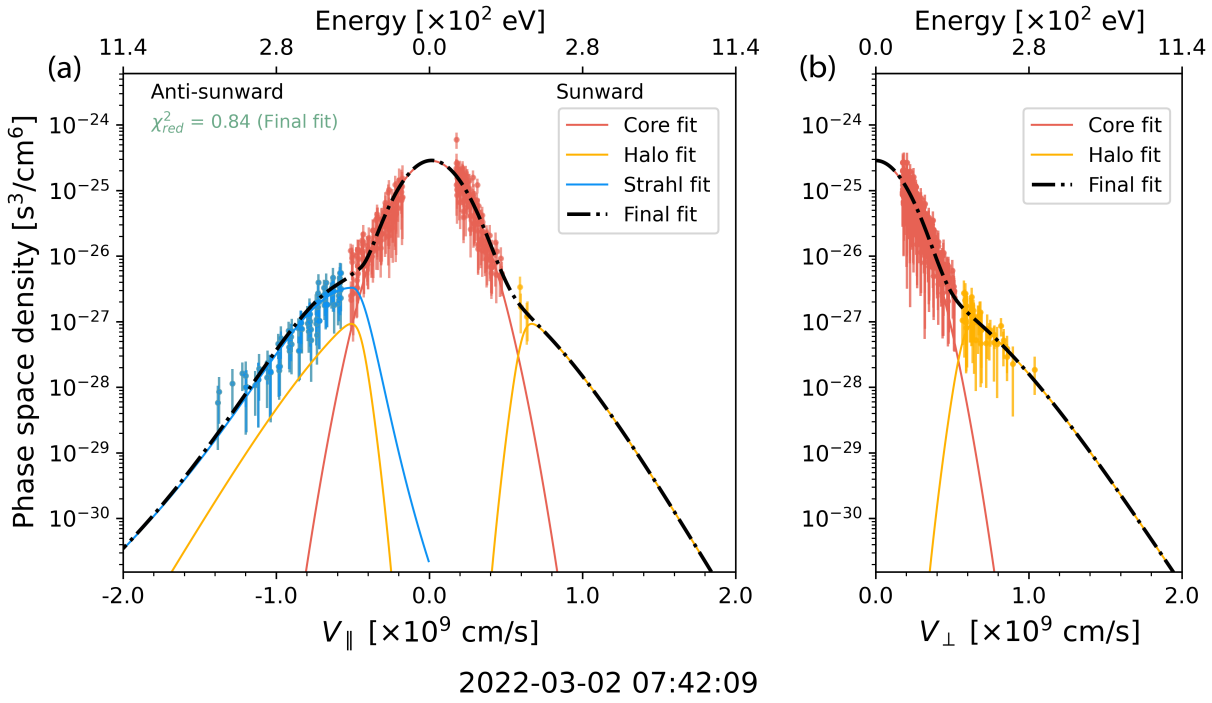

Figure 2. Example fit to an electron VDF from SO SWA-EAS at 07:42:09 UT on 2022 March 2. Panel (a) shows the parallel slice of the electron VDF; panel (b) shows the perpendicular slice. Solid lines depict the fitted models, and the points with error bars denote the measured VDF and their uncertainties. Core, halo, and strahl components are plotted in red, yellow, and blue, respectively. The black dashed curve is the combined model. The two-phase fitting routine successfully captures all components, with $\chi^2_{\rm red} = 0.84$ indicating a statistically good fit.

fitting problems. In the initial fitting phase, each electron component is fitted using the Adaptive Memory Programming for Global Optimization (AMPGO) method wrapped in lmfit. AMPGO is a hybrid global–local algorithm that enhances a standard local solver (e.g., least-squares minimization) by periodically exploring nearby parameter space. This helps avoid local minima and increases the chance of finding the global optimum (L. Lasdon et al. 2010). Although AMPGO is computationally expensive compared to purely local solvers, fitting each component separately reduces the number of free parameters and makes this approach efficient and robust, yielding reliable fits. In the final fitting phase, all parameters are refined simultaneously using the Levenberg–Marquardt algorithm (K. Levenberg 1944), which efficiently converges to a local minimum. This two-stage strategy balances robustness and speed, combining the global search capabilities of AMPGO for initialization with Levenberg–Marquardt's speed for final parameter refinement.

An example fit is illustrated in Figure 2. Solid curves depict each fitted model, while points with error bars represent the measured VDF and their uncertainties (σ_i in Equation (9)). The core, halo, and strahl components are identified using the method described above and are indicated in red, yellow, and blue, respectively, in both the model and the data. The fit captures each component well, and the combined model (black dashed line) closely follows the overall VDF, with $\chi^2_{\rm red} = 0.84$ indicating a good overall fit. Once the parameters are determined, the VDF of each component can be reconstructed. In particular, as $f_{\rm strahl}$ is a truncated bi-κ distribution, the strahl parallel temperature $T_{\rm strahl,\parallel}$ in this work is regarded as a representative, velocity-moment-based proxy for the characteristic parallel spread of the strahl VDF, rather than as an absolute thermodynamic temperature. We obtain $T_{\rm strahl,\parallel}$ by computing the second-order moment of $f_{\rm strahl}$:

$$T_{\rm strahl,\parallel} = \frac{m_e}{n_s k_{\rm B}} \int (v_\parallel - U_{s\parallel})(v_\parallel - U_{s\parallel}) f_s(\mathbf{v})\, d^3v \qquad (11)$$

where $U_{s\parallel}$ is the bulk velocity of the strahl in parallel direction derived from the first-order moment of $f_{\rm strahl}$, and $k_{\rm B}$ is the Boltzmann constant. We validate this definition using controlled tests on synthetic VDFs and compare it with the slope-derived temperature of L. Berčič et al. (2020). We find that the two approaches recover consistent trends when the strahl drift is very small, while explicitly allowing a finite $U_{s\parallel}$ provides a more robust temperature proxy when the strahl exhibits nonnegligible field-aligned drift. The core temperature $T_{\rm core,\perp}$ is calculated directly from the fitted thermal speed $v_{\perp \rm th,c}$.

3. Solar Wind Connectivity

We analyze SWA-EAS measurements recorded from 2022 March 2 to March 7 UT, the period of the Slow Solar Wind Connection Solar Orbiter Observing Plan (SOOP) conducted during SO's first perihelion passage. The solar wind sampled in this interval is accompanied by extensive coordinated remote-sensing observations, enabling a well-constrained analysis of the magnetic connectivity (S. L. Yardley et al. 2023, 2024). S. L. Yardley et al. (2024) combine (i) the potential field source surface (PFSS) with ballistic back-mapping to trace field lines from the spacecraft to the solar surface (A. P. Rouillard et al. 2020); (ii) the Extreme Ultraviolet Instrument High-Resolution Imager (EUI/HRI) and the Polarimetric and Helioseismic Imager High Resolution Telescope (PHI/HRT) on board SO to obtain the images and magnetic field of the predicted source regions; and (iii) the

Spectral Imaging of the Coronal Environment (SPICE) abundance diagnostics and SWA/HIS elemental compositions to verify the inferred sources. This multi-instrument approach (S. L. Yardley et al. 2024; Y. J. Rivera et al. 2025), in particular the demonstrated consistency between in situ and remote-sensing measurements, leads to the establishment of a trustworthy connection between the solar wind source and in situ properties.

Between 2022 March 2 and March 7, SO samples solar wind from three sections of the large equatorial coronal hole (CH1, CH2, and CH3) to two neighboring active regions (AR1 and AR2) (Figure 2 and 4 in S. L. Yardley et al. 2024). From 2022 March 2 to March 4, SO is immersed in three fast wind streams with shared properties of high proton velocity, increased proton temperature, and low Fe/O and C and O charge-state ratios. Transitions between the streams are marked by temporary magnetic field reversals, brief bursts of bidirectional strahl electrons, the inverted "U" shapes in the velocity-magnetic-field (V–B) correlation factor, signifying a brief loss of Alfvénicity due to magnetic sector crossings, and the small increases in Fe/O ratio, O^{7+}/O^{6+} and C^{6+}/C^{5+} charge-state ratios. Following the fast wind streams, SO detects an Alfvénic slow wind from the leading negative polarity of an active region (AR1). In situ heavy-ion data from SWA/HIS show increasing Fe/O and O^{7+}/O^{6+}, indicating a switch to hotter plasma with a coronal composition. This is independently verified by SPICE observations of the source region through the analysis of the Mg/Ne abundance ratio, which revealed a strong first ionization potential (FIP) effect (Figure 3 in S. L. Yardley et al. 2024). Finally, SO enters a stream with slower velocity, poor Alfvénic correlation and a decreasing Fe/O ratio back to photospheric levels. Changes in the in situ measurements are supported by PFSS result and SPICE observations. SO is connected to another active region (AR2) where SPICE also detects a weaker FIP effect (photospheric abundance).

S. L. Yardley et al.'s (2024) analysis cross-validates the magnetic connectivity between SO's in situ measurements and remote-sensing observations, providing a self-consistent result linking the solar wind streams to their coronal sources during this period. Therefore, we adopt the coronal source classification from that work, which segments the interval as follows: streams from CHs are sampled from March 2 00:00–21:00 UT (CH1), from March 2 21:40 UT to March 3 17:00 UT (CH2), and from March 3 18:00 UT to March 4 17:00 UT (CH3); slow wind measured between March 4 18:00 UT and March 5 20:00 UT originates from AR1, and between March 5 21:00 UT to March 7 00:00 UT is from AR2. These well-characterized source intervals form the basis of our analysis of the relationship between solar wind electron temperature and charge-state ratios within individual solar wind streams.

4. Observations

4.1. In Situ Measurements

Figure 3 displays the in situ measurements of the solar wind made by SO during the period of interest. Before March 4 18:00 UT, the velocity of the solar wind was predominantly over 500 km s^{-1} (panel (a)). After that, the solar wind speed gradually decreases. The three fast-wind streams are shaded blue, red, and green, whereas the two slow-wind intervals are shaded yellow and magenta. The radial component of the magnetic field shown in panel (b) was directed toward the Sun. Panel (c) shows the electron PAD in the SWA-EAS energy range of 50–2000 eV. Throughout this period, the strahl fluxes are significantly enhanced around 180°, consistent with antisunward propagation along inward-directed field lines. In panel (c), there are some transient changes in the strahl directions, associated with transitions across boundaries of the solar wind streams. Panel (d) shows the oxygen (red, O^{7+}/O^{6+}) and carbon charge-state (deep blue, C^{6+}/C^{5+}) ratios. The orange dashed line corresponds to an O^{7+}/O^{6+} value of 0.145, a criterion for distinguishing coronal hole wind (CHW) and noncoronal hole wind (NCHW) (L. Zhao et al. 2009). We note that both ratios increase over time, indicating a transition from cooler to hotter coronal source regions. Panels (e) and (f) display temperatures derived from our VDF fits: the core perpendicular temperature ($T_{\mathrm{core},\perp}$) and the proxy of strahl parallel temperature ($T_{\mathrm{strahl},\parallel}$). We use the core perpendicular temperature to avoid overlap with the strahl population in the electron VDF, allowing for a more reliable measure of its variation. We fit the VDF at 1 minute cadence, but the L3 SWA-HIS charge-state ratios are only available every 10 minutes. To align the two, we resample our fitted $T_{\mathrm{strahl},\parallel}$ and $T_{\mathrm{core},\perp}$ to each HIS timestamp using SciPy's shape-preserving piecewise-cubic Hermite interpolator (PCHIP; F. N. Fritsch & R. E. Carlson 1980; P. Virtanen et al. 2020). In panels (e) and (f), the lighter, semitransparent points show the original 1 minute temperatures, while the darker, opaque markers in the foreground are the PCHIP-interpolated values matched to the SWA-HIS time cadence. With these aligned data, we then examine their possible correlations. Comparing panels (a), (e), and (f), there is a clear anticorrelation between V_{sw} and $T_{\mathrm{core},\perp}$, with a Pearson correlation coefficient of $r = -0.72$ ($p < 0.001$). This behavior is consistent with measurements in the inner heliosphere by PSP (J. S. Halekas et al. 2020; M. Maksimovic et al. 2020a). Over the interval studied, we find no statistically significant association between V_{sw} and $T_{\mathrm{strahl},\parallel}$.

Figure 4 shows the overall correlation between the electron temperatures and the heavy-ion charge-state ratios during this period. Freeze-in electron temperatures from the CHIANTI database (K. P. Dere et al. 1997; E. Landi et al. 2013; A. R. Macneil et al. 2017) correspond to order-of-magnitude variations in heavy-ion charge-state ratios, so we compute the linear Pearson correlation r between each electron temperature and the logarithm of the charge-state ratio. The top two panels of Figure 4 plot strahl parallel temperature proxy $T_{\mathrm{strahl},\parallel}$ versus $\log_{10}(O^{7+}/O^{6+})$ and $\log_{10}(C^{6+}/C^{5+})$, respectively. We note a weak negative correlation between $T_{\mathrm{strahl},\parallel}$ and O^{7+}/O^{6+}, while no significant correlation is evident for $T_{\mathrm{strahl},\parallel}$ and C^{6+}/C^{5+}. The bottom two panels show the relationship of core temperature $T_{\mathrm{core},\perp}$ and charge-state ratios $\log_{10}(O^{7+}/O^{6+})$ and $\log_{10}(C^{6+}/C^{5+})$. In both cases, $T_{\mathrm{core},\perp}$ correlates positively with the charge-state ratios: $r = 0.71$ for oxygen and $r = 0.59$ for carbon, each with $p \ll 0.05$, indicating a strong, statistically significant association. In the bottom panels, it appears the data can be divided into two groups showing different correlation trends. Notably, the dividing value of O^{7+}/O^{6+} in panel (c) (orange dashed line) lies close to 0.145, which L. Zhao et al. (2009) identified as the threshold between the solar wind from CH and outside of the CH. For $O^{7+}/O^{6+} < 0.145$ (CHW), $T_{\mathrm{core},\perp}$ and O^{7+}/O^{6+} exhibit a positive correlation with $r = 0.50$ ($p \ll 0.05$). In

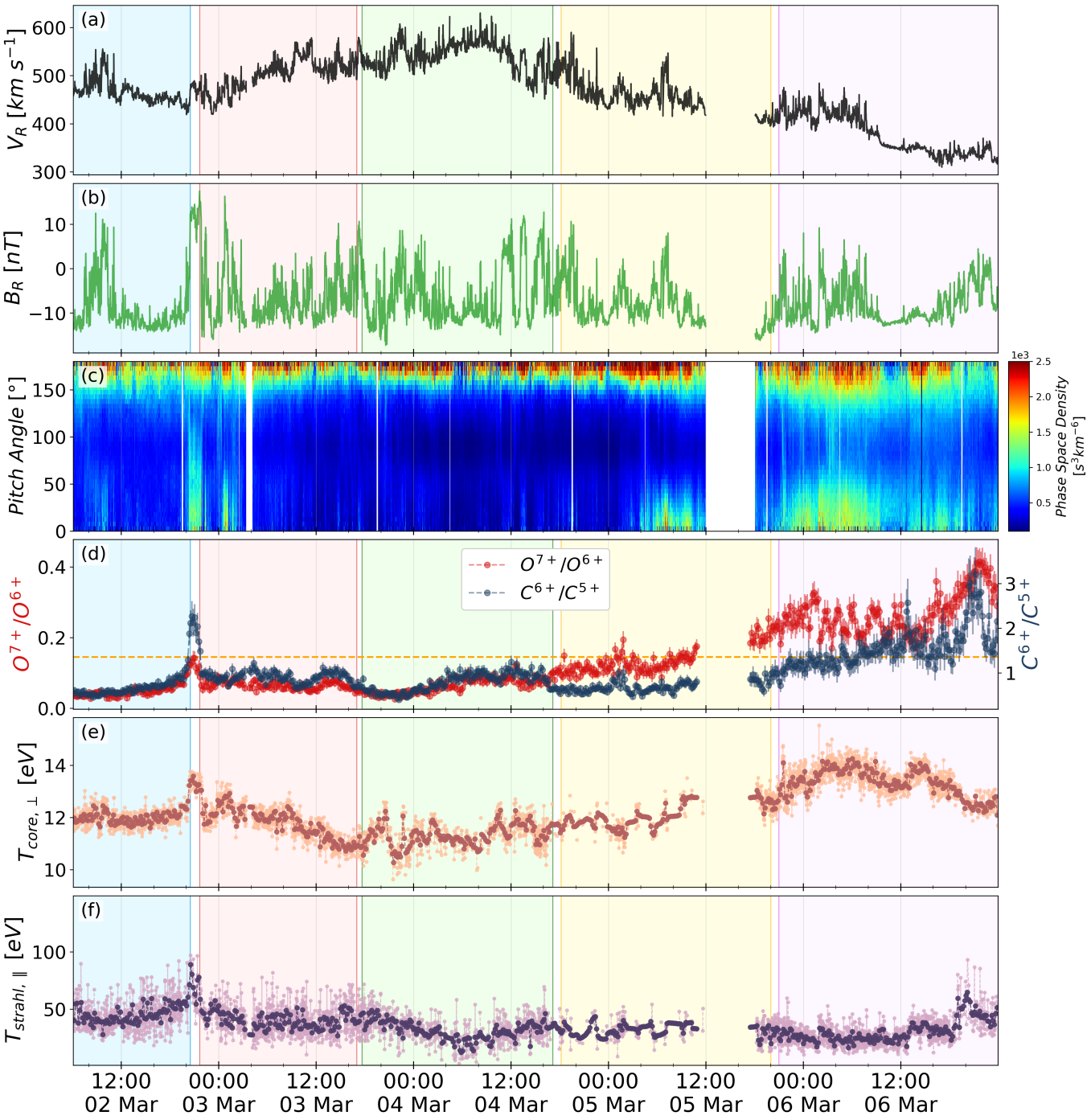

Figure 3. SO SWA and MAG measurements from 2022 March 2 to March 6. Streams from CH1, CH2, CH3, AR1, and AR2 are shaded in blue, red, green, yellow, and magenta. (a) Radial proton velocity V_R. (b) Radial component of the interplanetary magnetic field B_R. (c) Electron pitch-angle distribution, averaged over 50–2000 eV. The color represents phase space density. (d) Heavy-ion charge-state ratio measurements from SWA-HIS. Red markers denote O^{7+}/O^{6+}, and deep blue markers denote C^{6+}/C^{5+}. The orange dashed line denotes a discriminator value of 0.145 in the O^{7+}/O^{6+} ratio, distinguishing CHWs from NCHWs. (e) Fitted core perpendicular temperature $T_{core,\perp}$. (f) The proxy of strahl parallel temperature $T_{strahl,\parallel}$, derived from the second-order velocity moment of the fitted strahl component.

contrast, for $O^{7+}/O^{6+} > 0.145$ (NCHW), the association becomes significantly negative with $r = -0.65$ ($p \ll 0.05$).

4.2. Stream-resolved Relationships of Electron Temperature and Ion Charge-state Ratios

To explore how electron temperatures vary with ionic composition within individual streams identified by S. L. Yardley et al. (2024), we plot scatter diagrams of $T_{strahl,\parallel}$ and $T_{core,\perp}$ against oxygen and carbon charge-state ratios in Figures 5 and 6, respectively. Each stream is distinguished by color and symbol: blue circles, red squares, and green triangles represent plasma originating from CH1, CH2, and CH3, respectively; yellow diamonds correspond to AR1; and inverted purple triangles mark the stream associated with AR2. For each stream, we compute the Pearson correlation coefficients between the electron temperature and the charge-state ratios, and display them in corresponding colors.

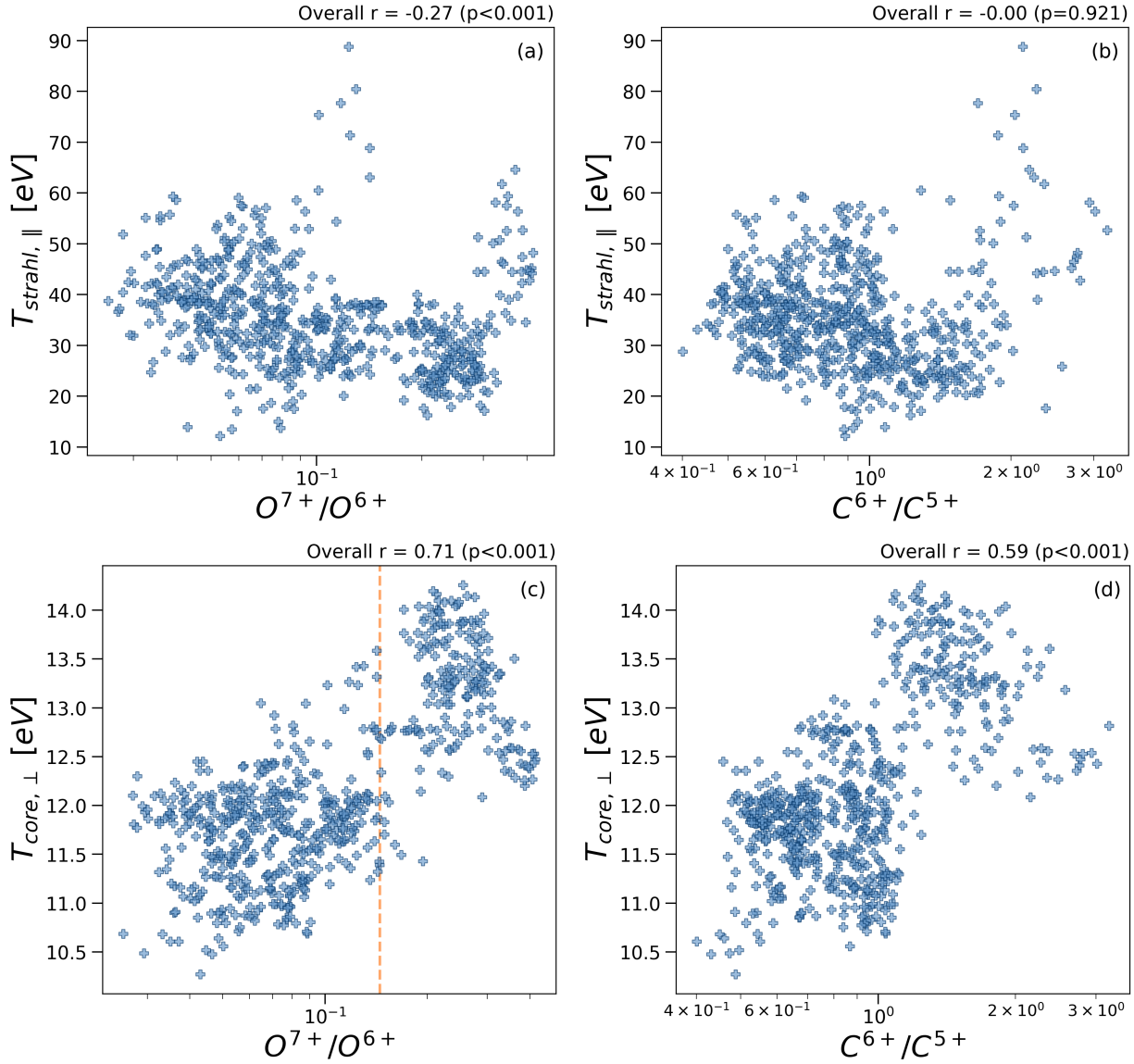

Figure 4. Correlations between electron temperature and the logarithm of charge-state ratios over the full interval. Panels (a) and (b) show $T_{\mathrm{strahl},\parallel}$ versus O^{7+}/O^{6+} and C^{6+}/C^{5+}, respectively. Panels (c) and (d) show $T_{\mathrm{core},\perp}$ versus O^{7+}/O^{6+} and C^{6+}/C^{5+}, respectively. The orange dashed line in panel (c) corresponds to a value of 0.145, the criterion distinguishing CHW and NCHW (L. Zhao et al. 2009). The Pearson correlation coefficient between the electron temperature and the logarithm of the charge-state ratio, with the p-value, is annotated in the top right of each panel.

Figure 5 presents the relationship between $T_{\mathrm{strahl},\parallel}$ and $\log_{10}(O^{7+}/O^{6+})$ (panel (a)), $\log_{10}(C^{6+}/C^{5+})$ (panel (b)). We note that data points are clustered by inferred solar wind origin, and the correlations observed within individual streams are clearly different from those calculated over the entire period. In panel (a), $T_{\mathrm{strahl},\parallel}$ exhibits a strong positive correlation with O^{7+}/O^{6+} in the streams from CH1 ($r = 0.68, p < 0.001$) and AR2 ($r = 0.56, p < 0.001$). By contrast, in the stream from CH3, a moderate negative correlation ($r = -0.38, p < 0.001$) is found. In panel (b), a similar positive correlation with C^{6+}/C^{5+} is observed in streams from CH1 ($r = 0.76, p < 0.001$) and AR2 ($r = 0.62, p < 0.001$), and a strong negative correlation is obtained in CH3 ($r = -0.52, p < 0.001$). For the remaining two intervals, i.e., CH2 and AR1, the p-values exceed 0.05, indicating no statistically significant correlation.

Figure 6 shows the correlation between $T_{\mathrm{core},\perp}$ and $\log_{10}(O^{7+}/O^{6+})$ (panel (a)), $\log_{10}(C^{6+}/C^{5+})$ (panel (b)). $T_{\mathrm{core},\perp}$ exhibits strong positive correlations in streams from CH1 ($r = 0.73, p < 0.001$) and AR1 ($r = 0.62, p < 0.001$), and a moderate positive correlation in the stream from CH2 ($r = 0.37, p < 0.001$). In contrast, for the stream from AR2, where $T_{\mathrm{strahl},\parallel}$ exhibits a significant positive correlation, $T_{\mathrm{core},\perp}$ has a strong negative correlation with O^{7+}/O^{6+} ($r = -0.65, p < 0.001$). For $T_{\mathrm{core},\perp}$ versus C^{6+}/C^{5+} (panel (b)), the correlations have similar behavior in streams from CH1 ($r = 0.79, p < 0.001$), CH3 ($r \sim 0.2, p < 0.05$), and AR2 ($r = -0.49, p < 0.001$). However, the correlations in the solar wind stream from CH2 become insignificant.

5. Discussion

Existing research at 1 au reports that only weak correlations are observed between the suprathermal electron temperature and heavy-ion charge-state ratios (A. R. Macneil et al. 2017; L. Yang et al. 2020). To investigate whether such correlation

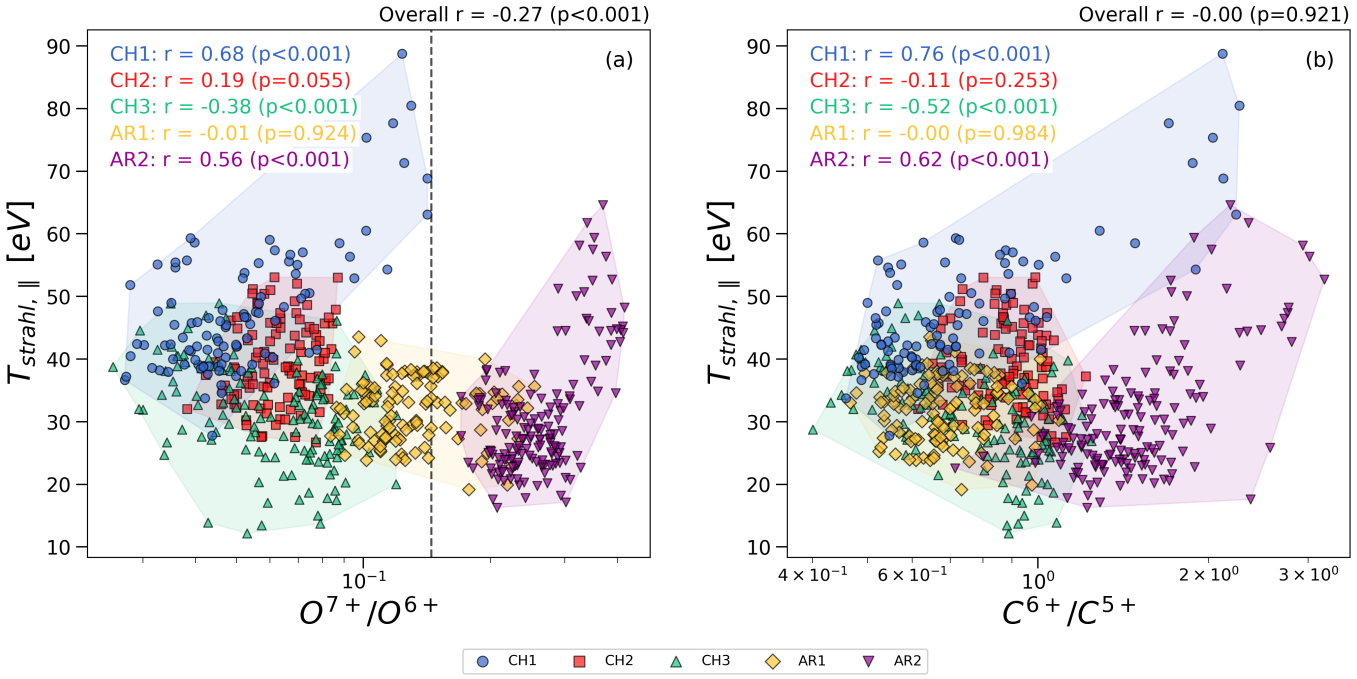

Figure 5. The correlation between $T_{\mathrm{strahl},\parallel}$ and charge-state ratios for individual streams. Blue circles, red squares, green triangles, yellow diamonds, and inverted purple triangles denote data from CH1, CH2, CH3, AR1, and AR2, respectively. Panel (a) plots $T_{\mathrm{strahl},\parallel}$ versus O^{7+}/O^{6+} with a black dashed vertical line at 0.145 marking the CHW/NCHW criterion. Panel (b) shows $T_{\mathrm{strahl},\parallel}$ versus C^{6+}/C^{5+}. The Pearson correlation coefficients for each stream are annotated in the corresponding color, and the overall correlation is displayed at the top of each panel.

exists or is eroded during transport, we analyze SO measurements at a closer radial distance, ∼0.5 au. In addition to comparing overall variations of in situ electron temperature and charge-state ratios, we quantify stream-resolved correlations so that electrons and ions potentially share a common solar origin, allowing a more accurate determination of their relationship.

5.1. Implications of Stream-resolved Correlations at 0.5 au

For the 5 day interval studied, correlations in individual streams are different from those obtained from the combined data. In panel (a) of Figure 5, except for the stream from CH3 having a similar result to the overall correlation, streams from CH1 and AR2 each show clear positive correlations, while CH2 and AR1 streams show no correlations. The scatterplots are well separated along the O^{7+}/O^{6+} axis and fall on either side of ∼0.145, consistent with previous studies identifying this O^{7+}/O^{6+} ratio as a discriminator between CHW and NCHW (L. Zhao et al. 2009; T. H. Zurbuchen et al. 2012; Y.-K. Ko et al. 2014). The distribution of data points from different streams leads to a negative overall correlation. In contrast, as C^{6+}/C^{5+} is measured to be less sensitive to the difference between CHW and NCHW, the data are less spread along it, and the overall correlation is not statistically significant. Although the carbon charge-state ratio provides an estimate of coronal electron temperature at a slightly lower freeze-in height than oxygen, it has been observed to correlate with oxygen over a large range of solar wind conditions (R. von Steiger 2008; R. von Steiger & T. H. Zurbuchen 2011). Therefore, the correlation trends derived from O^{7+}/O^{6+} and C^{6+}/C^{5+} are expected to be similar. This expectation holds true when examining individual solar wind (e.g., streams from CH1, CH3, and AR2) that exhibit statistically significant correlations. However, such consistent and stream-specific trends vanish once all streams are combined. In Figure 6, streams with significant correlations (i.e., streams from CH1 and AR2) also show consistent trends in both panels. Similar inconsistencies between the correlations obtained from the subsets and those derived from the complete dataset at 1 au are also reported by A. R. Macneil et al. (2017). They underscore that, although numerous subsets of data exhibit statistically significant correlations between suprathermal electron temperature and O^{7+}/O^{6+}, the statistical analysis of the complete dataset spanning 14 yr yields only weak to no residual correlations.

We attribute this discrepancy to stream mixing. Streams from different coronal regions undergo distinct processing in the corona and during propagation. In principle, the relationship between the electron temperature and heavy-ion charge-state ratios is set in the corona, while additional processes subsequently modify this relationship to varying degrees and may erase it. For example, transport effects may modify the strahl VDF continuously (M. J. Owens et al. 2008; Š. Štverák et al. 2009; J. B. Abraham et al. 2022). Whistler-mode waves can scatter strahl electrons in pitch angle and transfer their momentum from the parallel direction to perpendicular, leading to a broader pitch-angle width and lower parallel temperature (D. Verscharen et al. 2019; C. Cattell et al. 2021; V. K. Jagarlamudi et al. 2021; S.-Y. Jeong et al. 2022). Transient activities at the source, such as nanoflares or interchange reconnections, can also additionally modify the heavy-ion charge states or the VDF of suprathermal electrons (H. Che & M. L. Goldstein 2014; A. R. Macneil et al. 2020; I. Gershkovich et al. 2022). Combining diverse streams superposes different processes and inevitably dilutes or erases any stream-specific trend. The aggregate correlation thus reflects the relative fractions of "pristine" and "processed"

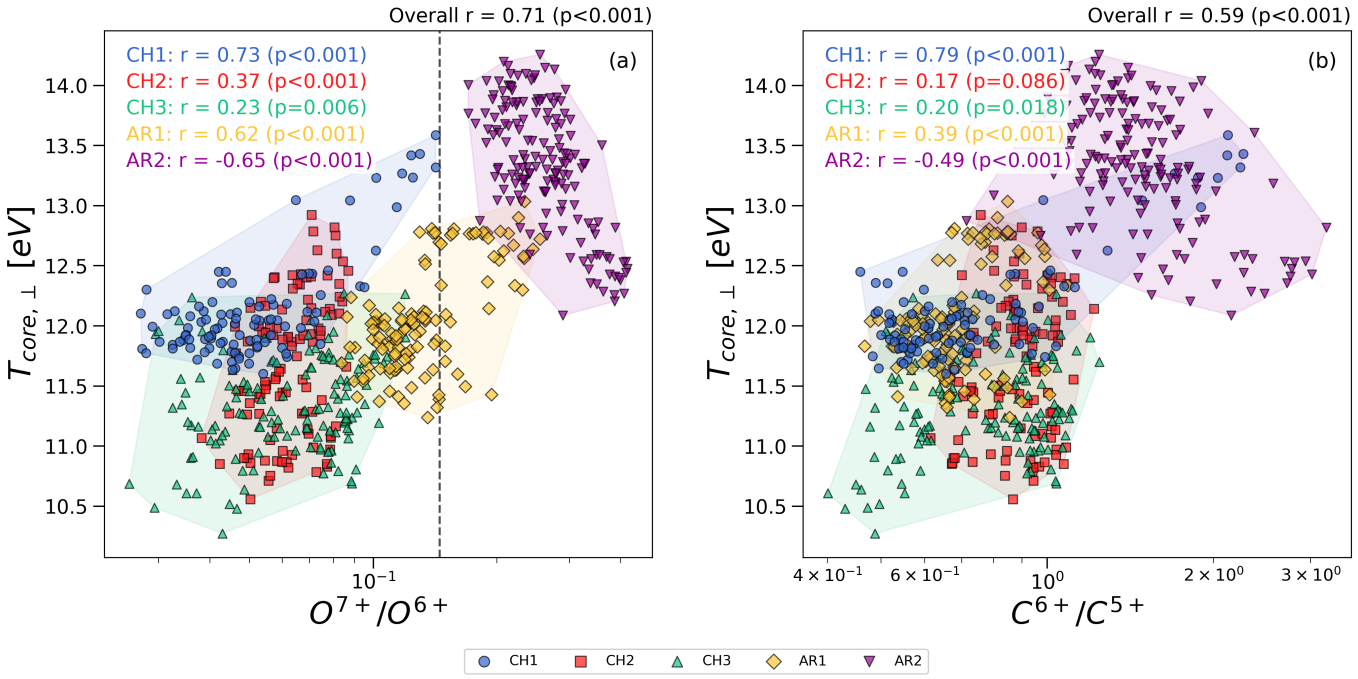

Figure 6. The correlation between $T_{\mathrm{core},\perp}$ and charge-state ratios for individual streams. Blue circles, red squares, green triangles, yellow diamonds, and inverted purple triangles denote data from CH1, CH2, CH3, AR1, and AR2, respectively. Panel (a) presents $T_{\mathrm{core},\perp}$ versus O^{7+}/O^{6+} with a black dashed vertical line at 0.145 denoting the CHW/NCHW criterion. Panel (b) plots $T_{\mathrm{core},\perp}$ versus C^{6+}/C^{5+}. The Pearson correlation coefficients for each stream are annotated in the corresponding color, and the overall correlation is shown at the top of each panel.

streams rather than a physical linkage. A robust assessment of electron temperature and charge-state ratios correlation should therefore respect the solar wind origin.

Stream-resolved analysis shows that the strahl parallel temperature proxy $T_{\mathrm{strahl},\parallel}$ correlates significantly with both O^{7+}/O^{6+} and C^{6+}/C^{5+} in some streams, whereas in other streams the relationship is weak or absent, confirming that $T_{\mathrm{strahl},\parallel}$ can carry the imprint of the coronal electron temperature but that subsequent processes can erase this signature. This indicates that, unlike heavy-ion charge-state ratios, $T_{\mathrm{strahl},\parallel}$ may not reliably serve as a universal proxy for solar wind source.

Additionally, the core perpendicular temperature $T_{\mathrm{core},\perp}$ shows a strong correlation with charge-state ratios. This relationship can be interpreted within the kinetic exospheric scenario. As illustrated in Figure 1, the boundary (dashed hyperbolas) between the trapped and ballistic electrons depends on the profile of magnetic field and electric potential (J. Lemaire & M. Scherer 1971; M. P. de Bonhome et al. 2025). At the exobase, the electron VDF contains only ballistic and escaping populations and reflects coronal conditions. Above the exobase, trapped electrons contribute to the VDF but lack a direct connection to the coronal source, and thus should retain no coronal information. Since the core population consists of both ballistic and trapped electrons, a strong correlation implies that ballistic electrons make the dominant contribution to $T_{\mathrm{core},\perp}$ and are mainly responsible for the heavy-ion freeze-in process. The extent of this imprint may depend on the relative positions of the exobase and the heavy-ion freeze-in height: when freeze-in occurs at or below the exobase, ballistic electrons are directly involved; above the exobase, trapped electrons emerge but electrons become sparse and collisionless, suppressing the ion charge-state evolution and limiting the role of the trapped population. Since the altitude of the exobase is determined by the magnetic field and the electric potential profiles, comparing its position with the freeze-in heights may help assess the relative contributions of ballistic and trapped electrons to the observed correlations. A limitation of the exospheric model is its neglect of collisions, which can scatter ballistic electrons into the trapped region of velocity space and thereby couple the trapped population to the Sun. Quantifying how near-Sun collisions modify $T_{\mathrm{core},\perp}$ and relating the exobase altitude to the species-dependent freeze-in heights require detailed modeling, which we defer to future work.

In Figure 6, for intervals where strahl strongly correlates with O^{7+}/O^{6+} ($|r| >= 0.5$), i.e., CH1 and AR2 streams, $T_{\mathrm{core},\perp}$ shows an even stronger correlation ($|r| \sim 0.7$). This may be because the core population is less affected by the scattering process driven by waves or turbulence than the strahl during propagation. Several studies have demonstrated an anticorrelation between $T_{\mathrm{core},\perp}$ and the solar wind speed V_{sw} (J. S. Halekas et al. 2020; M. Maksimovic et al. 2020a; C. S. Salem et al. 2023; C. Shi et al. 2023). Our observed correlation likely reflects the same underlying physics: solar wind streams from hotter coronal regions typically have lower velocities and higher heavy-ion charge-state ratios. Both the trends of $T_{\mathrm{core},\perp}$ and the charge-state ratios anticorrelate with V_{sw}, producing a positive correlation between them.

Comparing in situ electrons and ions measured at the same time implicitly assumes that the conditions of solar wind origin are quasi-steady or do not change drastically during the travel-time difference between them, so that both reflect similar coronal conditions. This assumption is generally safe for CHs as they can persist for several solar rotations (V. Heidrich-Meisner et al. 2017), while more caution is needed for ARs, which are more

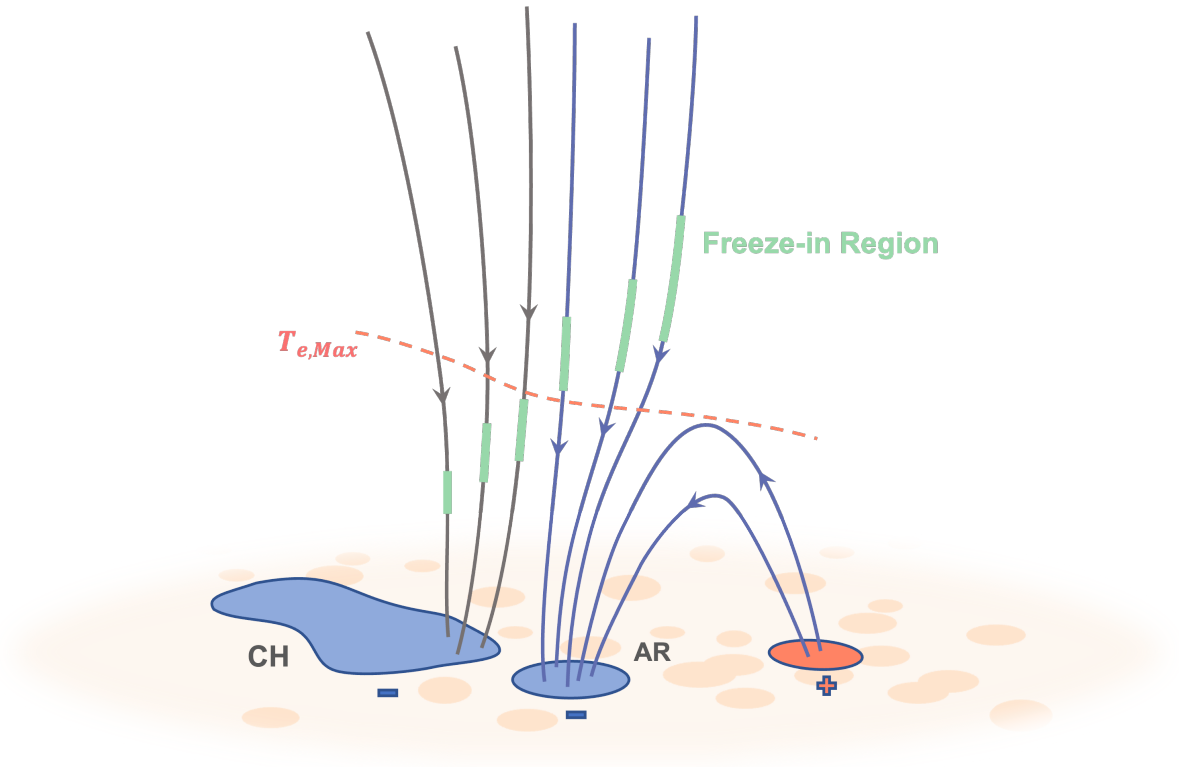

Figure 7. A schematic diagram illustrating freeze-in regions for different solar wind sources relative to the local electron-temperature maximum. The blue and orange shaded regions mark negative and positive polarity of the magnetic field footpoints on the photosphere. Blue lines with arrows show the magnetic field topology of the AR, while gray lines with arrows represent the open magnetic field from the CH. The dashed orange line indicates the altitude of the coronal peak temperature. Green segments along each field line mark the approximate freeze-in location for a given ion species.

variable, with the activity timescale ranging from hours to days (A. Bhargawa & A. K. Singh 2021; M. A. Weber et al. 2023). As core electrons travel more slowly than the strahl, their travel-time difference from the ions is smaller. Furthermore, the portion of the ballistic component reflected sunward from distant regions by the ambipolar potential follows a longer trajectory, thereby aligning its release time more closely with that of the heavy ions. These may explain why a correlation is observed between $T_{\mathrm{core},\perp}$ and O^{7+}/O^{6+} in the stream from AR1, while no correlation is found with $T_{\mathrm{strahl},\parallel}$. For CH1 and AR2 streams, significant correlations are present in both strahl and core temperature, suggesting that the assumption of a stable source is reasonable for these intervals.

Since the formation processes of the halo population remain actively debated and its properties can be modified during the propagation, we do not interpret the fitted halo temperature as a diagnostic of underlying coronal conditions. We, instead, examine whether the strahl-to-halo density ratio ($n_{\mathrm{strahl}}/n_{\mathrm{halo}}$) is related to the strength of stream-resolved correlations between $T_{\mathrm{strahl},\parallel}$ and the heavy-ion charge-state ratio. Comparing stream-averaged $n_{\mathrm{strahl}}/n_{\mathrm{halo}}$ with the corresponding Pearson correlation coefficients, we find no significant association within uncertainties. This indicates that halo-producing processes are unlikely to be the primary driver of the weak-correlation streams over the interval studied, consistent with recent PSP measurements suggesting that simple strahl scattering alone is insufficient to account for the observed halo population (I. Y. Vasko et al. 2019; J. S. Halekas et al. 2020; J. B. Abraham et al. 2022).

5.2. The Role of Freeze-in Height

In Figure 6, $T_{\mathrm{core},\perp}$ in both CH1 and AR2 streams strongly correlates with O^{7+}/O^{6+}, but with opposite signs. In the CH1 stream, $T_{\mathrm{core},\perp}$ rises with the charge-state ratio ($r = 0.73$, $p < 0.001$), while in AR2 it falls ($r = -0.65, p < 0.001$). This discrepancy likely reflects different coronal conditions at the freeze-in sites. It is well known that the freeze-in height of ions is governed by the electron temperature, density, and outflow speed (M. J. West et al. 2023). Oxygen and carbon charge states in fast and tenuous CH winds are frozen in closer to the Sun, typically between 1.1 and 1.9 R_{Sun} (Y.-K. Ko et al. 1997; Y. Chen et al. 2003; E. Landi et al. 2011), while their freeze-in heights become higher with the increase of electron density and the decrease of flow speed (Y.-K. Ko et al. 1999). Empirical models and observations suggest that the electron temperature in the inner corona has a local maximum, which differs for CHs and ARs (J. Geiss et al. 1995; S. R. Cranmer et al. 2007).

We therefore propose a scenario taking into account the relative location of the freeze-in height and the coronal electron temperature maximum to explain the differences in the correlation, as illustrated in Figure 7. The blue and orange zones respectively represent the negative polarity and the positive polarity of the magnetic field footpoints on the photosphere. The magnetic field lines rooted in CH and AR are colored gray and deep blue, respectively. The dashed line corresponds to an approximate location of coronal electron temperature maximum, and the green segments mark where ion charge-states freeze in. For a specific ion species, its freeze-in height in CH streams is relatively lower, whereas the freeze-in region in AR streams is higher and may exceed the

local electron-temperature maximum altitude due to higher electron density and slower outflow speed. When freeze-in occurs below the temperature maximum (CH streams in Figure 7), ions continue to ionize as the ambient electron temperature rises, yielding a positive correlation between the charge-state ratio and the freeze-in temperature. When the freeze-in region lies above the temperature maximum (AR streams in Figure 7), the ions still evolve toward higher charge states while the background temperature has begun to decline above the maximum, which will produce an anticorrelated relationship between them. This scenario provides a plausible explanation for the strong positive correlation in the CH1 stream and the strong negative correlation in the AR2 stream, based on observations and models of the heavy-ion ionization processes. It assumes that the freeze-in temperature tracks the local coronal temperature. In reality, the picture may be more complex due to nonequilibrium ionization in solar wind outflows (R. J. Edgar & R. Esser 2000; S. J. Bradshaw & H. E. Mason 2003; E. Landi et al. 2011; C. R. Gilly & S. R. Cranmer 2020). Resolving the actual mechanisms of this anticorrelation requires further study.

5.3. Radial Dependence of Correlations between Electron Temperature and Heavy-ion Charge-state Ratios

Our study demonstrates the presence of a strong correlation between electron temperatures and charge-state ratios at ~0.5 au, and identifies a difference between electron populations: the correlation is higher for the thermal core than for the suprathermal strahl. Closer to the Sun, a similar correlation between the electron temperature and charge-state ratios has been reported in joint PSP and SO observations on 2022 February 25 (Y. J. Rivera et al. 2024). The electron temperature derived from PSP/SPAN-e measurements (at 0.06 au) were found to highly correlate with the oxygen and carbon charge-state ratios measured by SO/HIS (at 0.6 au), yielding correlations $r = 0.93$ for O^{7+}/O^{6+} and $r = 0.87$ for C^{6+}/C^{5+}. Comparative studies at different heliocentric distances, including 0.06 au (Y. J. Rivera et al. 2024), 0.5 au (this study), and 1 au (A. R. Macneil et al. 2017), suggest that the correlation between solar wind electron temperatures and heavy-ion charge-state ratios may weaken with increasing heliocentric distance. This trend reflects the influence of transport-related processes such as wave–particle interactions, pitch-angle scattering, or turbulent diffusion, which progressively degrade the coronal imprint on the electron VDF as the solar wind expands. Based on this interpretation, we speculate that closer to the Sun, a greater number of solar wind streams will retain stronger and more consistent correlations between electron temperatures and heavy-ion charge-state ratios.

6. Conclusions

We have developed a two-stage fitting technique that reliably captures the core, halo, and strahl components of the electron VDF and applied it to SO SWA-EAS measurements at ~0.5 au over a 5 day period. This approach, together with the well-constrained magnetic connectivity of the observations from the slow solar wind connection science campaign (S. L. Yardley et al. 2024), allowed us to examine how solar wind electron temperatures relate to heavy-ion charge-state ratios stream by stream. We demonstrate that aggregating multiple streams masks stream-resolved correlations: when all intervals are combined, strongly correlated subsets are diluted by weak or uncorrelated ones, yielding misleading overall trends. Any robust comparison between electron temperatures and charge-state ratios should therefore respect the solar-wind source of a given stream.

We identify, for the first time inside 1 au, a clear correlation between the strahl parallel temperature proxy $T_{\mathrm{strahl},\parallel}$ and both oxygen (O^{7+}/O^{6+}) and carbon (C^{6+}/C^{5+}) charge-state ratios. Crucially, this imprint is not universal: some streams preserve a positive correlation (e.g., streams from CH1 and AR2), whereas others (streams from CH2 and AR1) show no significant link. The variability implies that coronal activities and transport processes can erode the coronal signature carried by the strahl before the plasma reaches 0.5 au. The stream-resolved analysis suggests that $T_{\mathrm{strahl},\parallel}$ may not reliably serve as a proxy of the solar wind origin.

Core electrons, notably, correlate more strongly with O^{7+}/O^{6+} and C^{6+}/C^{5+} than the strahl. We propose an interpretation of this correlation based on the exospheric model and suggest that ballistic electrons may play an important role in the heavy-ion freeze-in process. For the intervals studied, the correlation is positive in a CH wind stream (CH1) but strongly negative in an AR stream (AR2). We outline a scenario in which this sign reversal reflects the ion freeze-in height relative to the local maximum in the coronal temperature profile (Figure 7): freeze-in below the peak temperature (CH streams) produces a positive correlation, whereas above it (AR streams) yields a negative correlation. Our results underscore that the connectivity of solar wind electrons is more complicated than commonly assumed, and a comprehensive explanation will require combining global kinetics, local scattering, particle collisions near the Sun, and heavy-ion ionization processes.

Placing our results alongside those at 0.06 au (Y. J. Rivera et al. 2024) and 1 au (A. R. Macneil et al. 2017) suggests that correlation between in situ electron temperature and the coronal temperature may weaken with heliocentric distance, consistent with the cumulative action of scattering and turbulence during expansion. Further investigations are required to analyze SO perihelion measurements and coordinated PSP-SO intervals, which may help clarify how transport processes and source-region variability together shape the evolving linkage between solar-wind electrons and heavy-ion charge-state ratios.

Acknowledgments

X.W. acknowledges support from STFC through a PhD studentship (ST/Y509784/1). S.L.Y. is grateful to the Science Technology and Facilities Council for the award of an Ernest Rutherford Fellowship (ST/X003787/1). Solar Orbiter is a space mission of international collaboration between ESA and NASA, operated by ESA. Solar Orbiter Solar Wind Analyser (SWA) data are derived from scientific sensors that have been designed and created, and are operated under funding provided in numerous contracts from the UK Space Agency (UKSA), the UK Science and Technology Facilities Council (STFC), the Agenzia Spaziale Italiana (ASI), the Centre National d'Etudes Spatiales (CNES, France), the Centre National de la Recherche Scientifique (CNRS, France), the Czech contribution to the ESA PRODEX program, and NASA. Solar Orbiter SWA work at UCL/MSSL was funded under STFC grants ST/T001356/1, ST/S000240/1, ST/X002152/1, and ST/W001004/1.

ORCID iDs

Xiangyu Wu (吴翔宇) https://orcid.org/0000-0001-7019-5905
Christopher J. Owen https://orcid.org/0000-0002-5982-4667
Jesse Coburn https://orcid.org/0000-0002-2576-0992
Georgios Nicolaou https://orcid.org/0000-0003-3623-4928
Daniel Verscharen https://orcid.org/0000-0002-0497-1096
Jingting Liu (刘婧婷) https://orcid.org/0009-0003-9856-5949
Charalambos Ioannou https://orcid.org/0000-0003-4398-9931
Hao Ran (冉豪) https://orcid.org/0000-0002-8234-6480
Yeimy J. Rivera https://orcid.org/0000-0002-8748-2123
Stephanie L. Yardley https://orcid.org/0000-0003-2802-4381

References

Abraham, J. B., Owen, C. J., Verscharen, D., et al. 2022, ApJ, 931, 118
Bakrania, M. R., Rae, I. J., Walsh, A. P., et al. 2020, A&A, 639, A46
Berčič, L., Larson, D., Whittlesey, P., et al. 2020, ApJ, 892, 88
Bevington, P., & Robinson, D. K. 2003, Data Reduction and Error Analysis for the Physical Sciences (McGraw-Hill)
Bhargawa, A., & Singh, A. K. 2021, AdSpR, 68, 2643
Bochsler, P. 2007, A&ARv, 14, 1
Boe, B., Habbal, S., Druckmüller, M., et al. 2018, ApJ, 859, 155
Boldyrev, S., Forest, C., & Egedal, J. 2020, PNAS, 117, 9232
Bradshaw, S. J., & Mason, H. E. 2003, A&A, 401, 699
Cattell, C., Breneman, A., Dombeck, J., et al. 2021, ApJL, 911, L29
Che, H., & Goldstein, M. L. 2014, ApJL, 795, L38
Chen, Y., Esser, R., & Hu, Y. 2003, ApJ, 582, 467
Cranmer, S. R., van Ballegooijen, A. A., & Edgar, R. J. 2007, ApJS, 171, 520
de Bonhome, M. P., Pierrard, V., & Bacchini, F. 2025, A&A, 697, A104
Dere, K. P., Landi, E., Mason, H. E., Fossi, B. C. M., & Young, P. R. 1997, A&AS, 125, 149
Edgar, R. J., & Esser, R. 2000, ApJL, 538, L167
Esser, R., & Edgar, R. J. 2000, ApJL, 532, L71
Feldman, W. C., Asbridge, J. R., Bame, S. J., Gosling, J. T., & Lemons, D. S. 1978, JGR, 83, 5285
Feldman, W. C., Asbridge, J. R., Bame, S. J., Montgomery, M. D., & Gary, S. P. 1975, JGR, 80, 4181
Fritsch, F. N., & Carlson, R. E. 1980, SJNA, 17, 238
Geiss, J., Gloeckler, G., & Von Steiger, R. 1995, SSRv, 72, 49
Gershkovich, I., Lepri, S. T., Viall, N. M., Matteo, S. D., & Kepko, L. 2022, ApJ, 933, 198
Gilly, C. R., & Cranmer, S. R. 2020, ApJ, 901, 150
Halekas, J. S., Whittlesey, P., Larson, D. E., et al. 2020, ApJS, 246, 22
Hefti, S., Grünwaldt, H., Bochsler, P., & Aellig, M. R. 2000, JGRA, 105, 10527
Hefti, S., Zurbuchen, T. H., Fisk, L. A., et al. 1999, AIPC, 471, 495
Heidrich-Meisner, V., Peleikis, T., Kruse, M., Berger, L., & Wimmer-Schweingruber, R. 2016, A&A, 593, A70
Heidrich-Meisner, V., Peleikis, T., Kruse, M., Berger, L., & Wimmer-Schweingruber, R. F. 2017, A&A, 603, A84
Horaites, K., Boldyrev, S., & Medvedev, M. V. 2019, MNRAS, 484, 2474
Horbury, T. S., O'Brien, H., Blazquez, I. C., et al. 2020, A&A, 642, A9
Hundhausen, A. J., Gilbert, H. E., & Bame, S. J. 1968, ApJL, 152, L3
Jagarlamudi, V. K., de Wit, T. D., Froment, C., et al. 2021, A&A, 650, A9
Jeong, S.-Y., Abraham, J. B., Verscharen, D., et al. 2022, ApJL, 926, L26
Ko, Y.-K., Fisk, L. A., Geiss, J., Gloeckler, G., & Guhathakurta, M. 1997, SoPh, 171, 345
Ko, Y.-K., Gloeckler, G., Cohen, C. M. S., & Galvin, A. B. 1999, JGR, 104, 17005
Ko, Y.-K., Muglach, K., Wang, Y.-M., Young, P. R., & Lepri, S. T. 2014, ApJ, 787, 121
Landi, E., Alexander, R. L., Gruesbeck, J. R., et al. 2011, ApJ, 744, 100
Landi, E., Gruesbeck, J. R., Lepri, S. T., & Zurbuchen, T. H. 2012a, ApJ, 750, 159
Landi, E., Gruesbeck, J. R., Lepri, S. T., Zurbuchen, T. H., & Fisk, L. A. 2012b, ApJ, 761, 48
Landi, E., Young, P. R., Dere, K. P., Del Zanna, G., & Mason, H. E. 2013, ApJ, 763, 86
Lasdon, L., Duarte, A., Glover, F., Laguna, M., & Martí, R. 2010, COR, 37, 1500
Lemaire, J., & Scherer, M. 1971, PhFl, 14, 1683
Levenberg, K. 1944, QApMa, 2, 164
Lionello, R., Downs, C., Linker, J. A., et al. 2019, SoPh, 294, 13
Macneil, A. R., Owen, C. J., & Wicks, R. T. 2017, AnGeo, 35, 1275
Macneil, A. R., Owens, M. J., Beri, L., & Finley, A. J. 2020, MNRAS, 498, 5273
Maksimovic, M., Bale, S. D., Beri, L., et al. 2020a, ApJS, 246, 62
Maksimovic, M., Bale, S. D., Chust, T., et al. 2020b, A&A, 642, A12
Maksimovic, M., Pierrard, V., & Lemaire, J. 2001, Ap&SS, 277, 181
Maksimovic, M., Pierrard, V., & Riley, P. 1997, GeoRL, 24, 1151
Maksimovic, M., Zouganelis, I., Chaufray, J.-Y., et al. 2005, JGRA, 110, A09104
Meyer-Vernet, N., & Issautier, K. 1998, JGR, 103, 29705
Newville, M., Stensitzki, T., Allen, D. B., et al. 2016, Lmfit: Non-Linear Least-Square Minimization and Curve-Fitting for Python, Astrophysics Space Code Library, ascl:1606.014
Nicolaou, G., Wicks, R. T., Owen, C. J., et al. 2021, A&A, 656, A10
Owen, C. J., Abraham, J. B., Nicolaou, G., et al. 2022, Univ, 8, 509
Owen, C. J., Bruno, R., Livi, S., et al. 2020, A&A, 642, A16
Owens, M. J., Crooker, N. U., & Schwadron, N. A. 2008, JGRA, 113, A11104
Owocki, S. P., Holzer, T. E., & Hundhausen, A. J. 1983, ApJ, 275, 354
Pagel, C., Gary, S. P., de Koning, C. A., Skoug, R. M., & Steinberg, J. T. 2007, JGRA, 112, A04103
Pierrard, V., & Lemaire, J. 1996, JGR, 101, 7923
Pierrard, V., Maksimovic, M., & Lemaire, J. 1999, JGR, 104, 17021
Pilipp, W. G., Miggenrieder, H., Montgomery, M. D., et al. 1987, JGRA, 92, 1075
Riley, P., Lionello, R., & Rivera, Y. J. 2025, ApJ, 979, 204
Rivera, Y. J., Badman, S. T., Stevens, M. L., et al. 2024, ApJ, 974, 198
Rivera, Y. J., Badman, S. T., Verniero, J. L., et al. 2025, ApJ, 980, 70
Rivera, Y. J., Higginson, A., Lepri, S. T., et al. 2022, FrASS, 9, 417
Rouillard, A. P., Pinto, R. F., Vourlidas, A., et al. 2020, A&A, 642, A2
Salem, C. S., Pulupa, M., Bale, S. D., & Verscharen, D. 2023, A&A, 675, A162
Shi, C., Velli, M., Lionello, R., et al. 2023, ApJ, 944, 82
Štverák, Š., Herčí, D., Nicolaou, G., et al. 2025, A&A, 693, A185
Štverák, Š., Maksimovic, M., Trávníček, P. M., et al. 2009, JGRA, 114, A05104
Szente, J., Landi, E., & van der Holst, B. 2022, ApJ, 926, 35
Vasko, I. Y., Krasnoselskikh, V., Tong, Y., et al. 2019, ApJL, 871, L29
Verscharen, D., Chandran, B. D. G., Jeong, S.-Y., et al. 2019, ApJ, 886, 136
Virtanen, P., Gommers, R., Oliphant, T. E., et al. 2020, NatMe, 17, 261
Vocks, C., Salem, C., Lin, R. P., & Mann, G. 2005, ApJ, 627, 540
von Steiger, R. 2008, in The Heliosphere through the Solar Activity Cycle, ed. A. Balogh, L. J. Lanzerotti, & S. T. Suess (Springer), 41
von Steiger, R., & Zurbuchen, T. H. 2011, JGRA, 116, A01105
Weber, M. A., Schunker, H., Jouve, L., & Ik, E. 2023, SSRv, 219, 63
West, M. J., Seaton, D. B., Wexler, D. B., et al. 2023, SoPh, 298, 78
Yang, L., Wang, L., Zhao, L., et al. 2020, ApJL, 896, L5
Yardley, S. L., Brooks, D. H., D'Amicis, R., et al. 2024, NatAs, 8, 953
Yardley, S. L., Owen, C. J., Long, D. M., et al. 2023, ApJS, 267, 11
Zhao, L., Zurbuchen, T. H., & Fisk, L. A. 2009, GeoRL, 36, L14104
Zurbuchen, T. H., von Steiger, R., Gruesbeck, J., et al. 2012, SSRv, 172, 41